Lunar rare earth element distribution and ramifications for FeO and TiO_2: Lunar Prospector neutron spectrometer observations

R. C. Elphic, D. J. Lawrence, W. C. Feldman, B. L. Barraclough, Space and Atmospheric Sciences, Los Alamos National Laboratory, Los Alamos, New Mexico

S. Maurice, Observatoire Midi-Pyrénées, 31400 Toulouse, France

A. B. Binder, Lunar Research Institute, Tucson, Arizona

P. G. Lucey, Hawai'i Institute of Geophysics and Planetology, University of Hawai'i, Hawai'i

Abstract. Lunar Prospector neutron spectrometer data have been used to map the global surface distribution of the incompatible rare earth elements gadolinium and samarium from the low-altitude (30±15 km) mapping orbit. These results afford improved surface resolution and detailed views of the KREEP distribution within and around Mare Imbrium and elsewhere. Together with the Lunar Prospector gamma ray spectrometer results for thorium, the Gd and Sm results serve as a complementary and independent check of the distribution of KREEP on the Moon. The neutron spectrometer observations reflect the presence of Fe and Ti as well as Gd and Sm. The contributions of Fe and Ti are removed using high spatial resolution Clementine spectral reflectance determinations of FeO and TiO_2 abundances. Overall the resulting Gd and Sm abundance map agrees with the Th abundance map determined using the Lunar Prospector gamma ray spectrometer. In general the detailed features of the Procellarum/Imbrium KREEP terrane are found in both. For example, distinct highs in Gd, Sm, and Th abundances are resolved over the craters Mairan, Aristarchus, Kepler, Reinhold, Lalande and Aristillus, over the Apennine Bench and Fra Mauro regions and over the Montes Jura and Montes Carpatus, indicating an enhanced abundance of KREEP in these locations. The neutron observations also provide constraints on FeO and TiO_2 abundances; for some high-Ti locales, there is a significant disagreement with TiO_2 abundances inferred from Clementine spectral reflectance.

1. Introduction

It is believed that the Moon was born hot, the result of accretion of ejecta from a collision between the proto-Earth and a Mars-size body [*Hartmann and Davis,* 1975; *Cameron and Ward,* 1976]. The heat of formation resulted in a "magma ocean", a thoroughly molten outer layer as much as several hundreds of kilometers thick [*Warren,* 1985, and references therein]. As the

Moon cooled, crystallizing minerals either rose, sank, or remained in place depending on their density relative to the residual melt. Mafic minerals such as pyroxene and olivine formed the mantle, while light, aluminous silicates such as plagioclase feldspar floated to form the crust. As cooling and differentiation continued, the residual melt between the crust and mantle became increasingly enriched in incompatible elements, which do not readily fit into the crystal lattices of major silicate minerals. Crystallization of the final melt resulted in KREEP, materials enriched in these incompatible elements and named for potassium (K), rare earth elements (REE), and phosphorus (P) [*Hubbard et al.,* 1971; *Warren and Wasson,* 1979]. In the Apollo collection various amounts of the KREEP component are found in samples returned from all landing sites, but in greatest abundance from the Apollo 14 (Fra Mauro), Apollo 15 (Hadley-Apennines), and Apollo 12 (Oceanus Procellarum) sites.

Today the lunar highlands constitute the remnant of the ancient crust, while the floors of the large nearside impact basins have been flooded with basalts derived from partial melting of the upper mantle. Lunar surface rocks and soils largely fit into a mixture of three mineralogic and geochemical groups: feldspathic highlands materials, mafic mare basalt materials, and KREEP materials. The distribution of KREEP in surface rocks and soils is important because it bears on the evolution of the Moon during and following crustal formation. Surface expression of the KREEP component could derive from several possible mechanisms: (a) impacts large enough to excavate down to the original KREEP-rich zone between the crust and mantle; (b) exposure of regions of the crust that have been invaded by KREEP-rich fluids (excavation of KREEP-rich plutons in the crust); (c) basaltic volcanism incorporating KREEP while residing in a magma chamber or during transport to the surface. The geological context of KREEP-rich terrains provides information on what process (volcanism or impact basin formation) exposed or deposited these materials on the surface.

From lunar orbit, it is possible to infer the surface distribution of KREEP by measuring the abundance of thorium, a radioactive incompatible element highly correlated with REEs and potassium. Though limited in coverage, the Apollo gamma ray spectrometer (GRS) data hinted at a relative enrichment of KREEP in certain regions of the nearside, though farside highs near Van de Graff were also seen [*Metzger et al.,* 1977]. Recently, Lunar Prospector GRS observations of the entire Moon have revealed that the nearside Th-rich province is centered on Mare Imbrium; there is a much smaller secondary maximum near the Imbrium antipode on the northwestern ramparts of the South Pole-Aitken Basin [*Lawrence et al.,* 1998; *Lawrence et al.,* 1999]. The high Th abundances in and around Mare Imbrium, and the contrasting relative

paucity on the farside indicate a major hemispheric asymmetry in the composition of lower crust/upper mantle rocks. This result, in turn, suggests that early lunar differentiation must have been highly nonuniform throughout the Moon.

Lunar Prospector neutron spectrometer observations also suggest a similar surface distribution of REEs [*Elphic et al.* 1998]. The thermal neutron flux is lowest over the maria, due in large part to enhanced absorption by Fe and Ti, elements with large cross sections for thermal neutron capture. When corrected for the inferred abundance of Fe and Ti, based on spectral reflectance data from Clementine [*Blewett et al.*, 1997; *Lucey et al.*, 1998], the neutron data show residuals with anomalous absorption in the same regions as abundant Th. The residuals were ascribed to the presence of isotopes of gadolinium and samarium, rare earth elements that correlate well with other incompatible elements in the returned lunar samples. Thus, it is possible to obtain REE abundances using neutron spectrometer data provided the effects due to Fe and Ti can be removed.

In this paper we analyze neutron spectrometer data from the recent low-altitude phase (30±15 km) of the Lunar Prospector mission, which promises roughly three times better surface resolution than the earlier work. Like the approach of *Elphic et al.* [1998], we use the results of the analysis of Clementine spectral reflectance (CSR) data [*Lucey et al.*, 1998; *Blewett et al.*, 1997] which provides weight abundance estimates of FeO and TiO_2. The FeO and TiO_2 abundances in turn allow us to estimate the effect of Fe and Ti on thermal neutron spectrometer flux data, and remove it. The residual is then primarily due to Gd and Sm, which we map on the lunar surface to compare with the geological context. We can check agreement with the GRS Th map, and potentially come full circle and infer modifications to the FeO and TiO_2 abundances from CSR.

2. LP Neutron Data

2.1. Neutron Creation, Moderation, and Absorption

Neutrons are created within the lunar regolith through the impact of galactic cosmic rays that have typical energies of 1 GeV. The cosmic rays shatter the target nuclei into spallation products, including nucleons and larger nuclear fragments. This process forms a population of high-energy ("fast") neutrons, with characteristic energies between 1 and 8 MeV. Fast neutrons reflect the composition of the target materials: iron-rich mare basalt soils yield relatively more fast neutrons than iron-poor anorthosites [*Gasnault et al.*, 2000; *Maurice et al.*, 2000]. Fast neutrons interact with nuclei and lose energy through inelastic scattering. Below roughly 0.5

MeV ("epithermal" energies) the neutron flux tends to be relatively constant for different compositions, because even though iron-rich materials produce more fast neutrons, iron is also effective in down-scattering neutron energy. Thus the moderation process approximately offsets fast neutron production for the compositions of most lunar rocks and soils. For most major elements, the cross section for absorbing neutrons varies inversely as the neutron's speed. As moderation reduces the energy of epithermal neutrons toward the thermal range (< 0.3 eV), the cross section for absorption by nuclei increases. The absorption process for thermal neutrons is very composition dependent, because the thermal absorption cross section, σ_a, of certain elements such as iron and titanium is large, while for others it is small. Consequently, thermal neutron absorption is greater in mafic materials such as mare basalts than in iron-poor highlands rocks and soils. (However, calcium can also be a non-negligible absorber in plagioclase-rich materials).

These effects are illustrated in Figure 1, which shows simulated neutron flux spectra with energy for four distinct lunar compositions: a ferroan anorthosite, a KREEP basalt, the same KREEP basalt major element chemistry but lacking REEs, and a high-Ti mare basalt from Apollo 17 [cf. *Feldman et al.,* 2000]. The anorthositic composition is low in Fe, Ti or other strong absorber; consequently the flux of thermal neutrons is high. The KREEP basalt-like composition lacking REEs is considerably more mafic, and increased neutron absorption by Fe is evident below about 0.3 eV. The KREEP basalt with REEs shows an additional effect due to the presence of Gd and Sm, as described above. Finally, the high-Ti mare basalt shows the greatest absorption of all, due to the combined effect of abundant Fe and Ti. In contrast, note that the epithermal neutron fluxes are all approximately comparable, despite the disparate compositions. A companion paper discusses neutron genesis, moderation, and absorption in much greater detail [*Feldman, et al.,* 2000a].

The Lunar Prospector neutron spectrometer consists of two detectors [*Feldman et al.,* 1999]. A ^{3}He gas proportional counter tube covered with Sn detects all neutrons from thermal through epithermal energy range. A cadmium-covered ^{3}He tube detects only neutrons with energies above the cadmium thermal neutron capture resonance at about 0.3 eV; neutrons below this cutoff energy are absorbed in the Cd with high efficiency. Otherwise the two tubes have identical response, so the Sn-tube count rate minus the Cd-tube count rate yields an estimate of the thermal flux (E < 0.3 eV). The Cd tube provides a measure of the epithermal flux.

Figures 2a and 2b show global maps of the thermal and epithermal flux as measured by Lunar Prospector neutron spectrometer in the 30±15 km low-altitude orbit. The flux data were averaged in 2º pseudo-equal-area bins (2º in latitude, and with a longitudinal extent that varies roughly inversely with the sine of the latitude). As previously discussed by *Feldman et al.* [1998a] for high-altitude data, the thermal neutron map shows low fluxes over the nearside and farside maria, as well as over South Pole-Aitken (SPA) basin, Mare Australe region, the Schiller-Schickard region southwest of Mare Humorum, Tsiolkovsky, and the Mendel-Rydberg basin. Note also the local high in thermal neutron flux over Copernicus, as well as a broad high over the highlands north of SPA. The epithermal neutron map reflects many of the features of the thermal neutron map, but with far less dynamic range. Lower fluxes over the maria and SPA are apparent, as is the case with the thermal neutron flux, but the detailed structure of the lows in the western maria is different. In fact, the epithermal flux map already provides a hint of the REE absorption contributions that will emerge more clearly later. Lows at the north and south poles are also evident; these have been linked to the presence of hydrogen in polar shadowed regions [*Feldman et al.,* 1998b; 2000b]. The regional variations in the epithermal flux are much smaller (~10%) than those in the thermal flux (~ factor of 3), consistent with the comparative insensitivity of epithermal neutrons to composition (cf. Figure 1).

If Figure 1 demonstrates the importance of composition on thermal neutron flux, Figures 2a and b clearly suggest that we can obtain composition information from the neutron measurements. To do so we must understand the quantitative relationship between neutron fluxes and the scattering and absorbing character of the lunar regolith for different compositions.

2.2. The Macroscopic Absorption Cross Section, Σ_{eff}

Simulations of neutron transport and absorption have shown that there is a monotonic relationship between a material's ability to absorb thermal neutrons and the ratio of epithermal neutron flux to thermal neutron flux [*Feldman et al.,* 1991; see also *Feldman et al.,* 2000a]. This can be characterized by a material's macroscopic absorption cross section, Σ_{eff}, the weighted sum of all constituents' ability to absorb thermal neutrons:

$$\Sigma_{eff} = \sum_i \sigma_{ai} f_i N_A / A_i \qquad (1)$$

where σ_{ai} is the thermal neutron absorption cross section, f_i is the weight fraction, A_i is the atomic mass of constituent i, and N_A is Avogadro's number.

Table 1 shows the contributions of various elements to the total macroscopic absorption cross section for bulk regolith compositions from all Apollo landing sites, the Luna 16, 20, and 24 landing sites, and a ferroan anorthosite. Fe and Ti are the most important major element contributors to absorption in the mare soils; Fe is also the chief absorber (despite its low abundance) in the Apollo 16 highlands soil, but Ca is almost as important. Si, Al and the other major elements play a lesser, but non-negligible role in thermal neutron absorption.

The rare earth trace elements gadolinium and samarium have anomalously high cross sections for absorption of thermal neutrons [*Lingenfelter et al.,* 1972]. The isotopes ^{155}Gd, ^{157}Gd (14.7% and 15.7% of all Gd, respectively), and ^{149}Sm (13.8% of all Sm) have nuclear resonances which effectively increase the thermal neutron absorption cross sections, 58,000, 240,000 and 40,800 barns, respectively at 0.0253 eV (1 barn = 10^{-28} m^2) [*Lingenfelter et al.,* 1972]. In KREEP-rich materials the combined absorptive effect can be large even though these are trace elements. Consequently, the effects of these REEs are disproportionate to their low chemical abundances. Gadolinium and samarium can significantly affect Σ_{eff} in regions where they are relatively abundant (> 5 μg/g, see Table 1). Gd and Sm are most abundant in KREEP, along with other incompatible elements Th, K, and U. In the Apollo 14 soil the Gd and Sm contribution to neutron absorption is large fraction of the total from all other elements and increases Σ_{eff} from 50.8x10^{-4} to 79.4x10^{-4} cm^2/g [*Feldman et al.,* 1991]. For comparison, Sm and Gd contribute about 14% to the Apollo 11 mare Σ_{eff} value in Table 1.

The linear approximation to the monotonic relation from *Feldman et al.* [1999] is:

$$\Sigma_{eff} = 5.252\text{x}10^{-3} \cdot (f_{\text{epi}}/f_{\text{thermal}}) - 1.485\text{x}10^{-3} \qquad (2)$$

where f_{epi} and f_{thermal} are the measured epithermal and thermal neutron fluxes, respectively. This relationship comes from simulations of neutron transport in a wide variety of regolith compositions, and appears to hold when the observed values of $f_{\text{epi}}/f_{\text{thermal}}$ are compared to Σ_{eff}, based on known composition from returned samples. The $f_{\text{epi}}/f_{\text{thermal}}$ flux ratios used by *Feldman et al.* [1999] correspond to the actual responses of the LP NS detectors.

As discussed above and in *Elphic et al.* [1998], the thermal neutron absorption is due to the combined effect of all absorbers in the regolith, but primarily Fe, Ti, Gd and Sm. Because the Fe and Ti abundances vary so widely between highlands and maria, and even between mare basalts, we must take this variation into account and remove it in order to expose the effects of the REEs. The LP GRS results for Fe and Ti are in a preliminary state, so we will not use those data here.

Instead, we will exploit the near-global FeO and TiO_2 content inferred from Clementine spectral reflectance (CSR) data [*Blewett et al.,* 1997; *Lucey et al.,* 1998]. We construct an estimated value of Σ_{eff} based on the weight fraction of FeO and TiO_2 from the CSR data, and include an approximate contribution due to Ca as well as a constant background absorption due to all other species.

3. Clementine-Derived FeO and TiO_2: Estimating Σ_{eff}

The spectral reflectance techniques make use of an infrared absorption feature due to pyroxene and olivine to determine iron content, and a visible wavelength spectral slope due to opaque phases in the regolith to infer titanium abundance. The dominant opaque in the lunar samples is ilmenite, $FeTiO_3$. There is a correlation between TiO_2 abundance and the spectral opaque parameter in the returned samples, so this provides the means of determining titanium [*Lucey et al.,* 1995; 1996, 1998; *Blewett et al.,* 1997]. From these data it has been possible to infer the quantitative abundance of FeO and TiO_2 within ±70˚ latitude at resolutions approaching 100 m. These data were calibrated using lunar samples returned from a relatively small portion of the lunar nearside. Areas distant from the landing sites, such as the farside, might have different mineralogies - hence the inferred FeO and TiO_2 values might be less accurate. We use 0.5º resolution base maps of FeO and TiO_2.

We use the foregoing CSR-inferred FeO and TiO_2 abundance maps to construct an estimated Σ_{eff}. We exploit an empirical anticorrelation between FeO and CaO found in returned samples. This anticorrelation is principally due to variations in the abundance of the common lunar mineral anorthite plagioclase which is Ca-rich and Fe-poor. At higher FeO contents where the correlation flattens, the rock types are typically mare basalts which, while containing less plagioclase, contain other Ca-bearing minerals, particularly clinopyroxenes [*Haskin and Warren,* 1991].

We model the CaO dependence on FeO as follows:

$$\mathrm{CaO} = 20\ \mathrm{wt\%} - 0.91 \cdot \mathrm{FeO}, \qquad \mathrm{FeO} < 10\ \mathrm{wt\%} \tag{3a}$$

$$\mathrm{CaO} = 10.9\ \mathrm{wt\%}, \qquad \mathrm{FeO} \geq 10\ \mathrm{wt\%} \tag{3b}$$

This model broadly reproduces the variation of CaO with FeO, with a typical accuracy of about ±2 wt% CaO. There may be systematic deviations from this model with location. For example, the Apollo 12 mare basalt regolith and Apollo 15 and 17 picritic glasses would lie about 3 wt% below this model, while the Apollo 11 and Luna 16 regoliths would lie about 1 wt% higher than

the model [R. Korotev, personal communication]. However, Ca is not a strong thermal neutron absorber, and it is only significant when its net absorptive effect is comparable to that of Fe (in highlands soils). So systematic abundance errors are not significant in comparison to the uncertainties in Fe and Ti, or the effects of Gd and Sm, which we seek. In any case, we include such uncertainties in our error estimates below.

Let us construct a partial macroscopic absorption cross section, Σ^*_{eff}, using contributions from only FeO, TiO_2, and a model CaO, and compare that with the full Σ_{eff} constructed using contributions from all the major element oxides (but not REEs). The intent here is to find a way to estimate the true macroscopic absorption cross section (minus REEs) based only on FeO and TiO_2 abundances alone. Figure 3 is a plot of partial Σ^*_{eff} from FeO, TiO_2, and model CaO, versus the Σ_{eff} from all major-element oxides (but no REEs) for the returned sample soil and regolith breccia compositions and the ferroan anorthosite in Table 1. Clearly, we get an excellent estimate of the full, major-element Σ_{eff} from our partial Σ^*_{eff} – the least squares fit provides the relation:

$$\Sigma_{eff}\,(\text{no REEs}) = 0.951 \cdot \Sigma^*_{eff} + 17.5\text{x}10^{-4}\ \ (\text{cm}^2/\text{g}) \qquad (4)$$

If our estimate of major-element Σ_{eff} (no REEs) is accurate, then deviations from the ideal relationship in (2) should relate to additional absorbers, namely gadolinium and samarium.

We smooth the maps of Σ_{eff} (no REEs) with the approximate surface footprint of the LP neutron spectrometer in order to compare properly with the LP results. From the 30-km mapping orbit, the thermal neutron footprint has a full-width at half-maximum of about 110 km; the epithermal footprint is ~55 km at FWHM. We approximate the neutron spectrometer response footprints with gaussians of the same FWHM. The uncertainties in the CSR abundances are roughly ±1 - 2 wt% for FeO and perhaps somewhat larger for TiO_2 [*Lucey et al.,* 1998]. The spread in values of CaO wt% about the model in (3a) and (3b) based on returned samples is roughly ±2 wt%. These uncertainties lead to a conservative overall rms uncertainty in estimated Σ_{eff} of about $\pm 10.2\text{x}10^{-4}$ cm^2/g. The uncertainties in neutron spectrometer data consist partly of counting statistics, or roughly $1/N^{1/2}$, where N is the number of neutrons counted in a 32-sec accumulation period on Lunar Prospector, summed over all such periods for a given 2ºx2º spatial pixel. For example, the thermal neutron count rate ranges between 200 and 600 counts per 32-sec sample, and there are roughly 10 - 15 of these samples per 2ºx2º bin on average near the equator (the number of samples per bin goes up with latitude). Then there are between 2000 and

9000 counts per bin at the equator, depending on whether the location is in the highlands or the maria. The associated uncertainty in counting statistics thus ranges from 1% to 2% at the equator (more counts yields lower relative uncertainty). The counting uncertainty is even less at higher latitudes. Another source of uncertainty in the neutron data is the systematic error due to instrumental response, which we can estimate by checking the variations in count rates observed as Lunar Prospector revisits the same sub-spacecraft point again and again. The resulting calculated probable error of values within 2ºx2º pixels is approximately 1% for epithermal fluxes and 4% for thermals. Then the epithermal to thermal flux ratio $f_{\mathrm{epi}}/f_{\mathrm{thermal}}$ has an approximately 4.7% typical rms probable error overall, when counting statistics and systematic sources of uncertainty are folded together.

Figure 4 shows the estimated macroscopic absorption cross section Σ_{eff} (no REEs) from (4) versus the measured ratio of epithermal neutron flux to the thermal neutron flux, $f_{\mathrm{epi}}/f_{\mathrm{thermal}}$. Also shown is a gray line denoting the relationship of (2). If CSR estimates of FeO and TiO_2 (and inferred CaO abundances from the model of (3a) and (3b)) accounted for all the variations in Σ_{eff}, then the points would all fall on the ideal line. There is considerable scatter about this line, however, due to (a) possible errors in either the NS data and/or the CSR estimates and (b) other neutron absorbers in the regolith. (Bear in mind that uncertainties in Σ_{eff} are about $10\mathrm{x}10^{-4}$ cm^2/g, while probable errors in $f_{\mathrm{epi}}/f_{\mathrm{thermal}}$ are around 4.7%; hence little of the deviation from the ideal relationship can be explained by the Σ_{eff} uncertainty, but the errors in the flux ratio are much smaller than the scatter.) Based on the magnitude of the REE contributions seen in Table 1, we presume that the scatter below the ideal line is primarily due to additional neutron absorption from Gd and Sm. The difference, or $\Delta\Sigma_{eff}$ illustrated in Figure 4, is then the additional neutron absorption required to account for the observed neutron flux:

$$\Delta\Sigma_{eff} = 5.252\mathrm{x}10^{-3} \cdot (f_{\mathrm{epi}}/f_{\mathrm{thermal}}) - 1.485\mathrm{x}10^{-3} - \Sigma_{eff} \qquad (5)$$

Since we know the effective thermal absorption cross sections of Gd and Sm, we can estimate how much of these elements is needed to give $\Delta\Sigma_{eff}$. We note in passing that there are points above the ideal line of (3) in Figure 4. From (5), these yield negative values of $\Delta\Sigma_{eff}$, and correspond to overestimates of Σ_{eff}. In other words, we have additional information here that may help constrain the abundances of iron and titanium. This will be discussed in detail later.

Figure 5 is a global map of $\Delta\Sigma_{eff}$. Note the positive highs in $\Delta\Sigma_{eff}$ surrounding and within the Imbrium impact basin and Oceanus Procellarum, which we discuss in terms of enhanced REE

abundances in the next section. The negative lows of $\Delta\Sigma_{eff}$ are found in many of the maria, such as M. Tranquillitatis, southwestern and southeastern M. Serenitatis, northern M. Fecunditatis, M. Smythii, western M. Marginis, Tsiolkovsky, M. Moscoviense, Apollo, M. Orientale, western O. Procellarum, and M. Humorum. This association of mafic mare terrains with negative values of $\Delta\Sigma_{eff}$ is our main clue that there is a disagreement between the LP neutron data and CSR estimates of FeO or TiO_2 in these areas.

4. Distribution of REEs

If we assume that the ratio of Gd to Sm is approximately the mean of the values found in mafic impact melt breccias of the sample suite (~1.17 from *Korotev* [2000]), then $\Delta\Sigma_{eff}$ can be apportioned between the two REEs. For example, a $\Delta\Sigma_{eff}$ of 30×10^{-4} cm^2/g corresponds to a combination of 35.6 μg/g of Gd and 30.5 μg/g of Sm. Figure 6 is a map of $\Delta\Sigma_{eff}$ turned into the appropriate weight fraction of Sm, assuming the cosmic isotopic fractions for Sm. To estimate Gd abundances, multiply the Sm abundances by 1.17. In addition, we have reset all negative values of $\Delta\Sigma_{eff}$ to zero for clarity, and to avoid associating them with the Sm distribution. The Sm abundances range from values scattered about zero in the farside highlands north of SPA to highs exceeding ~40 μg/g Sm scattered around the periphery of the Imbrium impact basin. SPA also shows local highs (> 5 μg/g) in several spots on the northwestern rim of and within the impact basin. The global Sm map closely resembles the LP GRS low-altitude map of thorium, as shown in Figure 7 for comparison. A good correlation is expected for high concentrations of Th and the REEs, based on returned samples [*Haskin and Warren,* 1991; *Lawrence et al.,* 1999; *Korotev,* 2000].

Figure 8 focuses on the Sm abundances in and around Mare Imbrium. Here we can see that highs in REE abundances correlate with specific surface features: (1) Montes Jura to the north and northeast of Mare Imbrium (MJ, 50º to 55ºN, 14º to 34º W, 37 – 49 μg/g); (2) the crater Mairan (Mr, 41.6º N, 43.4º W, 37 - 49 μg/g); (3) the crater Aristarchus (Ar, 23.7ºN, 47.4ºW, 37 - 55 μg/g); (4) the crater Kepler (Kp, 8.1ºN, 38.0ºW, 37 - 49 μg/g); (5) hummocky terrain west of Copernicus (7 to 14N, 27W, 37 – 49 μg/g) and the Montes Carpatus (MC) north of Copernicus (Cp); (6) the crater Reinhold (Rn, 3.3ºN, 22.8ºW, 37 – 49 μg/g); (7) the Fra Mauro region (FM, 6.1ºN, 17.0ºW, 37 – 43 μg/g); (8) the crater Lalande (Ld, 4.4ºS, 8.6ºW, 37 - 43 μg/g); the crater Aristillus (As, 33.9ºN, 1.2ºE, 37 - 49 μg/g). There is also a local high over the Appenine Bench

(AB, 26ºN, 5ºW, 32 - 45 μg/g). Note the local (but subdued) high over the Montes Alpes region (46ºN, 1ºW, 26 - 32 μg/g).

It appears that impacts have excavated REE-rich materials in some locations, and not others. Highs over Mairan (Upper Imbrian), Aristarchus (Copernican), Kepler (Copernican), Reinhold (Eratosthenian), Aristillus (Copernican), and Lalande all point to exposure of KREEP-rich materials at these locations. Other Upper Imbrian craters within the Sinus Iridum ejecta blanket do not show the levels of REEs that Mairan does. More distal Copernicus ejecta to the north, west and south may bear enhanced KREEP, but certainly the proximal ejecta is locally lower in KREEP. Eratosthenes does not show excavation of enhanced KREEP, despite its location on the Imbrium impact basin rim. The rims and nearby ejecta of Plato (Upper Imbrian, 9ºW, 52ºN) and Archimedes (Upper Imbrian, 4.5ºW, 9.5ºN) appear to be local lows, because of flooding or embayment by later low-KREEP mare fill, because there was no KREEP-rich material below the surface there, or because of covering by later pyroclastic deposits [*Gillis and Jolliff*, 1999]. There are other craters such as Lambert (Eratosthenian) within Mare Imbrium (25.8ºN, 21.0ºW), of a similar size to Kepler but older, that have not excavated or exposed KREEP-rich materials. In part this is likely to be due to the depth of KREEP-rich material at various sites. Within Mare Imbrium, small craters may not excavate through the deeper mare fill overlying the (possibly) KREEP-rich Imbrium melt sheet or KREEP volcanics of the Appenine Bench Formation. But even small craters outside the Imbrium rim (Alpes Formation) may expose KREEP-rich materials, indicating shallower depth of burial there.

Many of the high-Sm abundance regions shown in Figure 8 are quite large, several tens of km on a side. This could result from either broad expanses with Sm abundances as high as is typically seen in KREEP in the sample suite (30 – 40 μg/g), or smaller regions with even higher concentrations. Very high values for REE abundances are found in only a few highland monomict rocks and polymict breccias in the returned samples; for example, quartz monzodiorite clasts in the Apollo 15 breccia 15405 (110 μg/g), a white clast in Apollo 14 breccia 14313 (259 μg/g). We do not suggest that the orbital data definitely indicate the exposure of highly evolved igneous rocks on the nearside, but the possibility of “KREEP ores” cannot be discounted.

However, one region of possible evolved igneous lithology has been identified by *Lawrence et al.* [1999] with a Th anomaly located in the northern farside highlands near the craters Compton (55ºN, 105ºE) and Belkovitch (60ºN, 100ºE). Elevated thorium abundances here of 2 – 4 μg/g contrast with otherwise typical highlands anorthosite composition, based on CSR data. Though not apparent in Figures 2a or 5, there is distinct evidence of thermal neutron absorption

due to Sm and Gd at this location. The magnitude of this effect in $\Delta\Sigma_{eff}$ corresponds to roughly 10 ± 5 μg/g of Sm and 12 ± 6 μg/g of Gd. These Th/REE ratios, together with low FeO, are consistent with a sizable region of alkali anorthosite composition, similar to 14047c [*Warren et al.*, 1983]. If the Th measurements were instead due to a small, unresolved patch of lunar "granite", such as 14321c, the REE levels would be too low for detection by the NS. Consequently the neutron spectrometer data favor an alkali anorthosite composition for the Compton-Belkovitch highlands anomaly.

5. Constraining FeO and TiO_2

In returned samples, high concentrations of incompatible elements are highly correlated. For example, in highland rocks, the correlation coefficient between Th and Sm is 0.99. Gd and Sm have a 0.998 correlation coefficient. Therefore we would expect a very good correlation between our inferred Sm abundances and Th abundances from the LP GRS. In Figure 9, we show a scatter plot of $\Delta\Sigma_{eff}$ versus Th abundance, as inferred from the LP gamma ray spectrometer [*Lawrence et al.*, 1999]. Also shown are green filled squares of measured Th abundance and the $\Delta\Sigma_{eff}$ corresponding to measured Gd and Sm abundances in selected KREEP samples from *Korotev* [2000], and a line denoting the trend for data described by *Taylor et al.* [1991]: KREEP basalts 15382 and 15386, quartz monzodiorite clast in 15405, basalt clasts in breccia 72275, average high-K KREEP from polymict breccias, and very high alumina polymict melt breccia 61156. There is a wide variation about an expected positive trend, especially for Th abundances between 1 and 5 μg/g. We have also color-coded two subsets: one for TiO_2 concentrations less than 1 wt%, and another for TiO_2 concentrations above 8 wt%. The low-TiO_2 subset should delineate the relationship between the REEs (as $\Delta\Sigma_{eff}$) and Th, and indeed a clear positive correlation emerges between $\Delta\Sigma_{eff}$ and Th abundance for this subset. However, the trend falls below that expected based on sample analysis, probably due to equation (2) not being quite the right relationship for the epithermal and thermal neutron measurements. The still-sizable scatter at low Th concentrations is likely to be partly due to the breakdown in REE-Th correlations in, for example, mare basalts [*Haskin and Warren*, 1991]. However, it is also clear that many of the negative $\Delta\Sigma_{eff}$ values correspond to high concentrations of Ti and Fe, as inferred from Clementine spectral reflectance. We suspect that points to the left of the blue, low-Ti trend have smaller values of estimated $\Delta\Sigma_{eff}$ due to overestimates in TiO_2 and FeO abundance, which corresponds to an overestimate of Σ_{eff} from (1).

We can examine this question in another way. Figure 10 plots $\Delta\Sigma_{eff}$ versus CSR-derived TiO_2 abundance, with $\Delta\Sigma_{eff}$ now in units of the TiO_2 weight percent needed to give the observed value of $\Delta\Sigma_{eff}$. Once again there is considerable scatter, partly due to the offsetting effects of positive absorption due to Gd and Sm, and apparent overestimates of TiO_2 abundance. To help distinguish these competing effects, we make a subset of points, selected for Th < 2 μg/g so that the contributions of Gd and Sm should be small, less than the equivalent of 2 wt% of TiO_2. This subset reveals that there is a systematic negative trend of $\Delta\Sigma_{eff}$ (in equivalent TiO_2 wt%) with CSR-derived TiO_2 abundance. In other words, these data suggest that some of the CSR TiO_2 (and possibly FeO) abundance values have been overestimated; the magnitude of this effect is equivalent to about a -5 wt% correction for an estimated 10 wt% and above of TiO_2.

The focus here is on CSR-derived TiO_2 to explain these effects because titanium's absorption cross section is more than twice that of iron, and an order of magnitude greater than that of calcium (see Table 1). But there may be a significant contribution due to overestimates in FeO as well. A preliminary comparison of CSR FeO and Lunar Prospector GRS FeO suggests that the CSR FeO values may also be too high in some locations [*Lawrence et al.*, 1999a], by as much as 3 or 4 wt% within some of the nearside maria. A 4 wt% overestimate in FeO would lead to an error in Σ_{eff} of about ~8×10^{-4} cm^2/g; a 4 wt% overestimate in TiO_2 would lead to an error of ~18×10^{-4} cm^2/g in Σ_{eff}. To achieve the magnitude of the $\Delta\Sigma_{eff}$ deficit in Figure 9 with iron alone, errors of greater than 12 wt% in FeO would be required. Such an error seems highly unlikely given the uncertainties of the spectral reflectance technique used to obtain FeO abundance. The results in Figures 9 and 10 suggest that better agreement would be obtained if the CSR FeO abundances in low-Th regions were reduced by 2 – 4 wt%, and CSR TiO_2 abundances in these regions were reduced by 3 – 5 wt%. This would be a challenge to the results of *Blewett et al.* [1997] and *Lucey et al.* [1998a], who used resolved images of Apollo and Luna sample sites to constrain the inferred TiO_2 abundances with uncertainties no greater than about ±2 wt%. The disagreement would still be present if other spectral techniques were used to infer TiO_2 abundances.

There may be other explanations for the apparent overabundance of TiO_2 that we infer from LP neutron data. It is possible that unknown instrumental effects cause the measured values of the epithermal to thermal neutron flux ratio to differ from the theoretical values of the flux ratio that give us equation (2). In this case the ideal line shown in Figure 4 would not be the correct baseline for determining $\Delta\Sigma_{eff}$. The adjusted ideal line could be steeper, reducing the negative

values of $\Delta\Sigma_{eff}$ that we interpret as being due to TiO_2 anomalies (thus removing the TiO_2 problem). We doubt that this is the cause of the problem, because such a slope change also increases the positive values of $\Delta\Sigma_{eff}$ that we attribute to Gd and Sm. The resulting higher values of REE abundances are then just as problematic, in the sense that they are much larger than we expect based on measured global Th abundance, and on the Th-REE geochemistry in returned samples. For example, in regions where Th abundance is around 9 μg/g, we would infer a Gd abundance of over 70 μg/g, and a Sm abundance of over 60 μg/g. This is almost a factor of 2 greater than expected based on returned samples of KREEP. While it is possible that the Th-REE correlation found in returned highland samples does not represent the relationship for the bulk lunar surface, such a good correlation is expected on geochemical and petrologic grounds.

We also note that the results of *Gasnault et al.* [1999] and *Maurice et al.* [1999] indicate that the Lunar Prospector fast (0.5 – 8 MeV) neutron data also suggest that the CSR estimates of TiO_2 may be too high to explain their fluxes. Simulations of nuclear processes show that fast neutron yield is a weighted linear combination of all species. Both Ti and Fe are especially effective at producing fast neutrons (have larger weights), and have comparable weights. Consequently, fast neutron fluxes are higher over the maria than over the highlands, and are especially enhanced over high-Ti mare regions such as Mare Tranquillitatis. However, when compared with the CSR FeO and TiO_2 abundances, the predicted and observed fast neutron fluxes have the best agreement when the TiO_2 weighting function is half the value obtained from the nuclear simulations. In other words, the nominal CSR TiO_2 abundances lead to an overprediction of fast neutron flux over high-Ti mare basalts. The fast neutron results come from a completely different sensor (the gamma ray spectrometer) than the epithermal and thermal neutron results. Thus, the TiO_2 implications described in this paper and those described by *Maurice et al.* [1999] are completely independent, but both reflect an apparent disagreement with TiO_2 abundance estimates obtained through UV/VIS spectral reflectance techniques.

The major assumptions concerning the CSR method of *Blewett et al.*, [1997] and *Lucey et al.* [1999] for mapping titanium are that: 1) variations in opaque mineral abundance overwhelmingly dominate variations in the UV/VIS color because of their nature as dark, spectrally neutral absorbers; 2) opaque minerals are the principle carriers of TiO_2. The empirical nature of the calibration is such that if the abundance of other minerals or soil components with important UV/VIS properties are correlated with either TiO_2 abundance, or soil maturity, the technique will include these color variations in the calibration from spectral parameter to elemental abundance, and at the same time will suppress maturity effects. Thus for example, accumulation of

spectrally red Fe-Ti bearing glass as a Ti-rich soil matures will be correlated with optical maturity, which is minimized by the CSR technique. Systematic violation of these assumptions, especially systematically different behavior than between Apollo landing site color-elemental behavior, will give rise to systematic errors in TiO_2 abundance. The presence of abundant low-Ti opaques, Ti-rich pyroxenes, systematic variations in pyroclastic glass content from mare to mare, or variation in Ti^{3+}-Ti^{4+} ratio in glasses or minerals could all be responsible for color-reflectance properties different from the landing site sample stations used by, for example, *Blewett et al.* [1997]. The differences between the CSR estimates of TiO_2 and these NS measurements have the potential to shed important light on partitioning of TiO_2 among different phases, much as this work has led to the ability to directly map the abundance of REE. At present, this apparent disagreement in TiO_2 abundances remains an area of active analysis, with no obvious resolution.

A final point concerns inferred FeO abundances. The $\Delta\Sigma_{eff}$ map (Figure 5) for most of the highlands outside the Imbrium/Procellarum KREEP terrain and high-Ti basalts is nearly featureless. Therefore, in regions low in thorium and titanium the Σ_{eff} estimated from CSR data (which is dominated by the CSR FeO estimate) is in good agreement with the neutron spectrometer results, in part validating the CSR FeO estimates. Differences between CSR estimates of farside FeO and the Apollo GRS experiment Fe measurements [*Davis*, 1980] have been noted [*Clark and Mcfadden*, 1996; *Clark and Basu*, 1998; *Clark and Mcfadden*, this volume]. The Apollo GRS data show strong variations in Fe on the lunar farside not associated with South Pole-Aitken basin. The lack of detection of these variations by the CSR experiment has prompted the suggestion that the Fe variations observed by Apollo are due to variations in the abundance of olivine to which they claim the CSR technique is insensitive. Our results show that the LP neutron spectrometer did not detect the variations in Fe suggested by the Apollo GRS experiment, and so there is no need to invoke “hidden” olivine in the farside highlands.

References

Blewett, D. T., P. G. Lucey, B. R. Hawke, and B. L. Jolliff, Clementine images of lunar sample-return stations: Refinement of FeO and TiO_2 mapping techniques, *J. Geophys. Res., 102*, 16,319, 1997.

Cameron, A. G. W., and W. Ward, The origin of the Moon (abstract), in *Lunar Science VII*, pp. 120-122, Lunar Science Institute, Houston.

Clark P. E., and A. Basu, Pyroxene vs. total iron ratios reflected in spectral reflectance and gamma-ray observations, *Lunar Planet Sci., XXIX*, 1998

Clark P. E., and L. A. Mcfadden, The lunar crust as a case study: a comparison of iron data derived from geochemical and mineralogical remote sensing techniques, *Lunar Planet Sci., XXVII*, 227-228, 1996.

Clark P. E., and L. A. Mcfadden, New results and implications for lunar crustal iron distribution using sensor data fusion techniques, *J. Geophys. Res.*, this volume.

Davis, P. A., Iron and titanium distribution on the Moon from orbital gamma-ray spectrometry with implications for crustal evolutionary models, *J. Geophys. Res., 85*, 3209-3224, 1980.

Elphic, R. C., D. J. Lawrence, W. C. Feldman, B. L. Barraclough, S. Maurice, A. B. Binder, and P. G. Lucey, Lunar Fe and Ti abundances: Comparison of Lunar Prospector and Clementine data, *Science, 281*, 1493, 1998.

Feldman, W. C., R. C. Reedy, and D. S. McKay, Lunar neutron fluxes as a function of composition and hydrogen content, *Geophys. Res. Lett., 18*, 2157, 1991.

Feldman, W. C., B. L. Barraclough, S. Maurice, R. C. Elphic, D. J. Lawrence, D. R. Thomsen, and A. B. Binder, Major compositional units of the Moon: Lunar Prospector thermal and fast neutrons, *Science, 281*, 1489, 1998a.

Feldman, W. C., S. Maurice, A. B. Binder, B. L. Barraclough, R. C. Elphic, and D. J. Lawrence, fluxes of fast and epithermal neutrons from Lunar Prospector: Evidence for water ice at the lunar poles, *Science, 281*, 1496, 1998b.

Feldman, W. C., B. L. Barraclough, K. R. Fuller, D. J. Lawrence, S. Maurice, M. C. Miller, T. H. Prettyman, and A. B. Binder, The Lunar Prospector gamma-ray and neutron spectrometers, *Nucl. Instr. and Meth., A422*, 562-566, 1999.

Feldman, W. C., D. J. Lawrence, R. C. Elphic, D. T. Vaniman, D. R. Thomsen, B. L. Barraclough, S. Maurice, and A. B. Binder, The chemical information content of lunar thermal and epithermal neutrons, *J. Geophys. Res., this issue?*, 2000.

Feldman, W. C., B. L. Barraclough, S. Maurice, R. C. Elphic, D. J. Lawrence, D. R. Thomsen, and A. B. Binder, Lunar polar hydrogen deposits, *J. Geophys. Res., this issue?*, 2000.

Gasnault, O., C. d'Uston, W. C. Feldman, and S. Maurice, Lunar fast neutron leakage flux calculation and its elemental abundance dependence, *submitted to J. Geophys. Res.*, 2000.

Gillis, J. J., and B. L. Jolliff, Lateral and vertical heterogeneity of thorium in the Procellarum KREEP Terrane: As reflected in the ejecta deposits of post-Imbrium craters, in *Workshop on New Views of the Moon II: Understanding the Moon Throughout the Integration of Diverse Datasets*, LPI Contribution No. 980, Lunar and Planetary Institute, Houston, 1999.

Hartmann, W. K., and D. R. Davis, Satellite sized planetesimals and lunar origin, *Icarus, 24*, 504-554, 1975.

Haskin, L. A., and P. H. Warren, Lunar chemistry, in *Lunar Sourcebook*, Heiken, Vaniman, and French, eds., (Cambridge University Press, New York, 1991), pp. 357 - 474.

Hubbard, N. J., C. Meyer, Jr., P. W. Gast, H. Wiesmann, The compoistion and derivation of Apollo 12 soils, *Earth Planet. Sci. Lett., 10*, 341-350, 1971.

Korotev, R. L., The great lunar hot spot and the composition and origin of the Apollo mafic ("LKFM") impact-melt breccias, *J. Geophys. Res., in press*, 2000.

Lawrence, D. J. W. C. Feldman, B. L. Barraclough, A. B. Binder, R. C. Elphic, S. Maurice and D. R. Thomsen, Global elemental maps of the Moon: The Lunar Prospector Gamma-ray Spectrometer, *Science, 284*, 1484, 1998.

Lawrence, D. J., W. C. Feldman, B. L. Barraclough, R. C. Elphic, S. Maurice, A. B. Binder, and P. G. Lucey, Iron abundances on the Moon as seen by the Lunar Prospector gamma-ray spectrometer. In *Workshop on New Views of the Moon II: Understanding the Moon Throughout the Integration of Diverse Datasets.* LPI Contribution No. 980, Lunar and Planetary Institute, Houston, 1999a.

Lawrence, D. J., W. C. Feldman, B. L. Barraclough, A. B. Binder, R. C. Elphic, S. Maurice, M. C. Miller, and T. H. Prettyman, High resolution measurements of absolute thorium abundances on the lunar, *Geophys. Res. Lett., 26*, 2681-2684, 1999b.

Lingenfelter, R., E. H. Canfield, V. E. Hampel, The lunar neutron flux revisited, *Earth and Planet. Sci. Lett., 16*, 355, 1972.

Lucey, P. G., G. J. Taylor, E. Malaret, Abundance and distribution of iron on the moon, *Science, 268*, 1150, 1995.

Lucey, P. G., D. T. Blewett, J. R. Johnson, G. J. Taylor, B. R. Hawke, Lunar titanium content from UV-VIS measurements, (abstract) *Lunar Planet. Sci. XXVII*, 781, 1996.

Lucey, P. G., D. T. Blewett, B. R. Hawke, Mapping the FeO and TiO_2 content of the lunar surface with mulispectral imagery, *J. Geophys. Res., 103*, 3679, 1998a.

Lucey, P. G., G. J. Taylor, B. R. Hawke, and P. D. Spudis, FeO and TiO_2 concentrations in the South Pole-Aitken basin: Implications for mantle composition and basin formation, *J. Geophys. Res., 103*, 3701, 1998b.

Maurice, S., W. C. Feldman, D. J. Lawrence, O. Gasnault, C. d'Uston, and P. G. Lucey, High-energy neutrons from the Moon, *J. Geophys. Res., this issue*, 2000.

Taylor, G. J., P. Warren, G. ryder, J. Delano, C. Pieters, and G. Lofgren, Lunar rocks, in *Lunar Sourcebook*, Heiken, Vaniman, and French, eds., (Cambridge University Press, New York, 1991), p. 183 - 284.

Warren, P. H., The magma ocean concept and lunar evolution, *Annu. Rev. Earth Planet. Sci, 13*, 201-240, 1985.

Warren, P. H., G. J. Taylor, K. Keil, G. W. Kallemeyn, P. S. Rosener, and J. T. Wasson, Sixth foray for pristine nonmare rocks and an assessment of the diversity of lunar anorthosites, *Proc. Lunar Planet. Sci. Conf. 13th*, in *J. Geophys. Res., 88*, A615-A630, 1983.

Warren, P. H., and J. T. Wasson, The origin of KREEP, *Rev. Geophys. Space Phys., 17*, 73 – 88, 1979.

R. C. Elphic, D. J. Lawrence, W. C. Feldman, B. L. Barraclough, Space and Atmospheric Sciences, Los Alamos National Laboratory, Los Alamos, NM 87545 USA
S. Maurice, Observatoire Midi-Pyrénées, 31400 Toulouse, France
A. B. Binder, Lunar Research Institute, University of Arizona Science and Technology Park, Suite 2360, 9040 South Rita Road, Tucson, AZ 85747
P. G. Lucey, Hawai'i Institute of Geophysics and Planetology, University of Hawai'i, HI 96822 USA

Figure Captions

Figure 1. Thermal and epithermal neutron flux-versus-energy spectra corresponding to four distinct surface compositions: a ferroan anorthosite, KREEP basalt with no REE contribution, KREEP basalt including REEs, and a high-Ti mare basalt. The neutron flux in the epithermal range is less sensitive to composition than the thermal flux.

Figure 2. (a) Global map of the thermal neutron flux from the Lunar Prospector low altitude (30±15 km) mapping orbit. Note the lows over the nearside maria (dark outlines near map's center) and over South Pole-Aitken basin on the farside (SPA), and the highs over the mid-latitude farside highlands. (b) Global map of the epithermal flux from the low-altitude mapping orbit. The relative variation in epithermal flux is far smaller than that in thermal flux.

Figure 3. The relationship between the true macroscopic absorption cross section, Σ_{eff}, (minus REEs) and estimated Σ^*_{eff} based on FeO, TiO_2, and a model for CaO alone. The actual value of Σ_{eff} (no REEs) can be estimated with high confidence from Σ^*_{eff} alone.

Figure 4. Estimated Σ_{eff} (no REEs) based on Clementine-derived FeO, TiO_2, and modeled CaO, and the relationship shown in Figure 3, versus the epithermal-to-thermal neutron flux ratio. The gray line denotes the ideal relationship of (2). Deviations of Σ_{eff} below this ideal relationship, $\Delta\Sigma_{eff}$ as shown, indicate the need for additional neutron absorbers (Gd and Sm). Points above the line may be symptomatic of overestimates of major element neutron absorbers FeO and/or TiO_2.

Figure 5. Global map of $\Delta\Sigma_{eff}$. Enhancements of the additional (unaccounted for) neutron absorption are largely found on the nearside, around Mare Imbrium. Note also that negative values of $\Delta\Sigma_{eff}$, denoting overestimates in major element neutron absorbers FeO, TiO_2, or CaO, are found in many of the maria (dark outlines on the nearside).

Figure 6. Global, two-hemisphere map of inferred samarium abundance. Negative values of $\Delta\Sigma_{eff}$ have been reset to zero for clarity and to optimize the dynamic range for Sm abundance. Note that highs of 45 – 51 μg/g can be found in several locations within and around M. Imbrium.

Figure 7. Thorium abundance on a two-hemisphere map projection, similar to Figure 6. Note the excellent correspondence between thorium and inferred samarium highs in the Imbrium/Procellarum regions.

Figure 8. Inferred Sm abundances for the Imbrium/Procellarum regions. "Hot spots" of high Sm concentrations are found associated with several impact craters (see text for notations), and general highs also correspond to features of the Apennine Bench and the Fra Mauro region.

Figure 9. $\Delta\Sigma_{eff}$ versus thorium concentration. Blue points correspond to a low-Ti subset (TiO_2 < 1 wt%), and red points to a high-Ti subset (TiO_2 > 8 wt%). Note that the low-Ti subset yields a good correlation between Th and $\Delta\Sigma_{eff}$. The high-Ti subset suggests that overestimates in TiO_2 abundances are responsible for negative values of $\Delta\Sigma_{eff}$. The red line denotes the trend observed in selected KREEP samples for Th versus Sm [*Taylor et al.*, 1991].

Figure 10. $\Delta\Sigma_{eff}$, recast as equivalent TiO_2 wt%, versus CSR-derived TiO_2 content. Blue points correspond to a low-Th subset, in which we expect little or no REE-contribution to $\Delta\Sigma_{eff}$. For this subset, a clear inverse trend again suggests that the absorbing effect of Ti has been overestimated, i.e., CSR-derived TiO_2 abundance estimates may be too high to account for the LP neutron observations.

Table 1. Composition and macroscopic absorption cross section for returned samples*

Comp.	Apollo 11 wt%	$\sigma_a f N_A/A$	Apollo 12 wt%	$\sigma_a f N_A/A$	Apollo 14 wt%	$\sigma_a f N_A/A$	Apollo 15 wt%	$\sigma_a f N_A/A$	Apollo 16 wt%	$\sigma_a f N_A/A$
SiO_2	41.99	6.76	46.21	7.44	48.10	7.74	47.19	7.60	44.89	7.23
TiO_2	7.94	34.77	2.61	11.43	1.70	7.44	1.46	6.39	0.53	2.32
Al_2O_3	12.58	3.42	12.13	3.30	17.40	4.73	14.32	3.89	27.23	7.41
FeO	16.40	34.83	17.19	36.51	10.40	22.09	14.98	31.82	4.98	10.58
MgO	7.93	0.75	10.42	0.99	9.40	0.89	10.95	1.04	6.00	0.57
CaO	11.74	5.81	9.85	4.88	10.70	5.30	10.47	5.18	14.56	7.21
Na_2O	0.47	0.46	0.41	0.40	0.70	0.69	0.40	0.39	0.47	0.46
MnO	0.21	2.41	0.21	2.32	0.13	1.46	0.19	2.09	0.07	0.74
Sm	1.38e-03	4.37	1.51e-03	4.78	2.87e-03	9.09	0.00	0.00	0.00	0.00
Gd	1.80e-03	10.28	1.70e-03	9.71	3.50e-03	20.00	1.56e-03	8.91	0.00	0.00
CaO model	10.90	5.40	10.90	5.40	10.90	5.40	10.90	5.40	15.47	7.66
Σ_{eff}		103.90		81.76		79.44		67.32		36.51
Σ_{eff} no REE		89.24		67.26		50.35		58.41		36.51
Σ_{eff}*		75.00		53.34		34.93		43.61		20.56

*$\sigma_a f N_A/A$ is in units of 10^{-4} cm^2/g

Table 1 (continued)

Comp.	Apollo 17 wt%	$\sigma_a f N_A/A$	Luna 16 wt%	$\sigma_a f N_A/A$	Luna 20 wt%	$\sigma_a f N_A/A$	Luna 24 wt%	$\sigma_a f N_A/A$	FAN wt%	$\sigma_a f N_A/A$ (cm^2/g)
SiO_2	44.47	7.16	44.37	7.14	45.20	7.28	45.40	7.31	44.20	7.12
TiO_2	2.84	12.44	3.30	14.45	0.50	2.19	1.04	4.55	0.13	0.57
Al_2O_3	18.93	5.15	15.68	4.26	22.75	6.19	11.95	3.25	33.30	9.06
FeO	10.29	21.86	16.75	35.58	7.46	15.84	19.55	41.52	1.91	4.06
MgO	9.95	0.94	8.78	0.83	9.69	0.92	9.87	0.94	0.84	0.08
CaO	12.29	6.08	11.50	5.69	14.70	7.28	11.07	5.48	19.02	9.41
Na_2O	0.43	0.42	0.35	0.34	0.39	0.38	0.28	0.28	0.60	0.59
MnO	0.16	1.81	0.21	2.32	0.10	1.18	0.25	2.84	0.00	0.00
Sm	7.48e-04	2.37	8.29e-04	2.63	3.18e-04	1.01	1.96e-04	0.62	0.00	0.00
Gd	1.01e-03	5.77	1.06e-03	6.06	4.40e-04	2.51	0.00	0.00	0.00	0.00
CaO model	10.90	5.40	10.90	5.40	13.22	6.54	10.90	5.40	18.26	9.04
Σ_{eff}		64.00		79.31		44.78		66.79		30.88
Σ_{eff} no REE		55.86		70.63		41.26		66.17		30.88
Σ_{eff}*		39.69		55.42		24.58		51.47		13.67

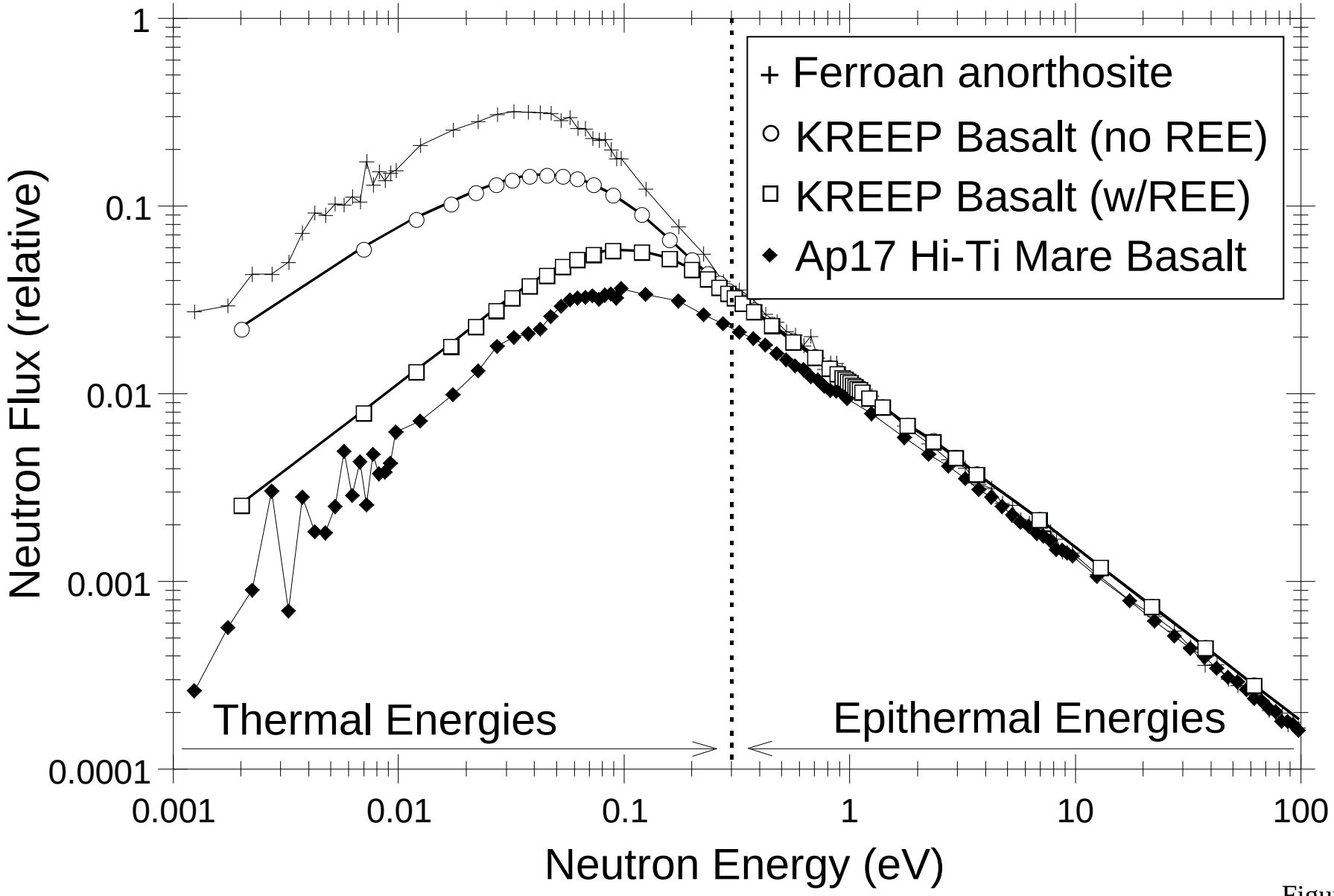
Neutron Flux (relative)
1
0.1
0.01
0.001
0.0001
0.001
0.01
0.1
1
10
100
Neutron Energy (eV)
+ Ferroan anorthosite
○ KREEP Basalt (no REE)
□ KREEP Basalt (w/REE)
◆ Ap17 Hi-Ti Mare Basalt
Thermal Energies
Epithermal Energies

Figure 1

Thermal Neutron counts/32 sec

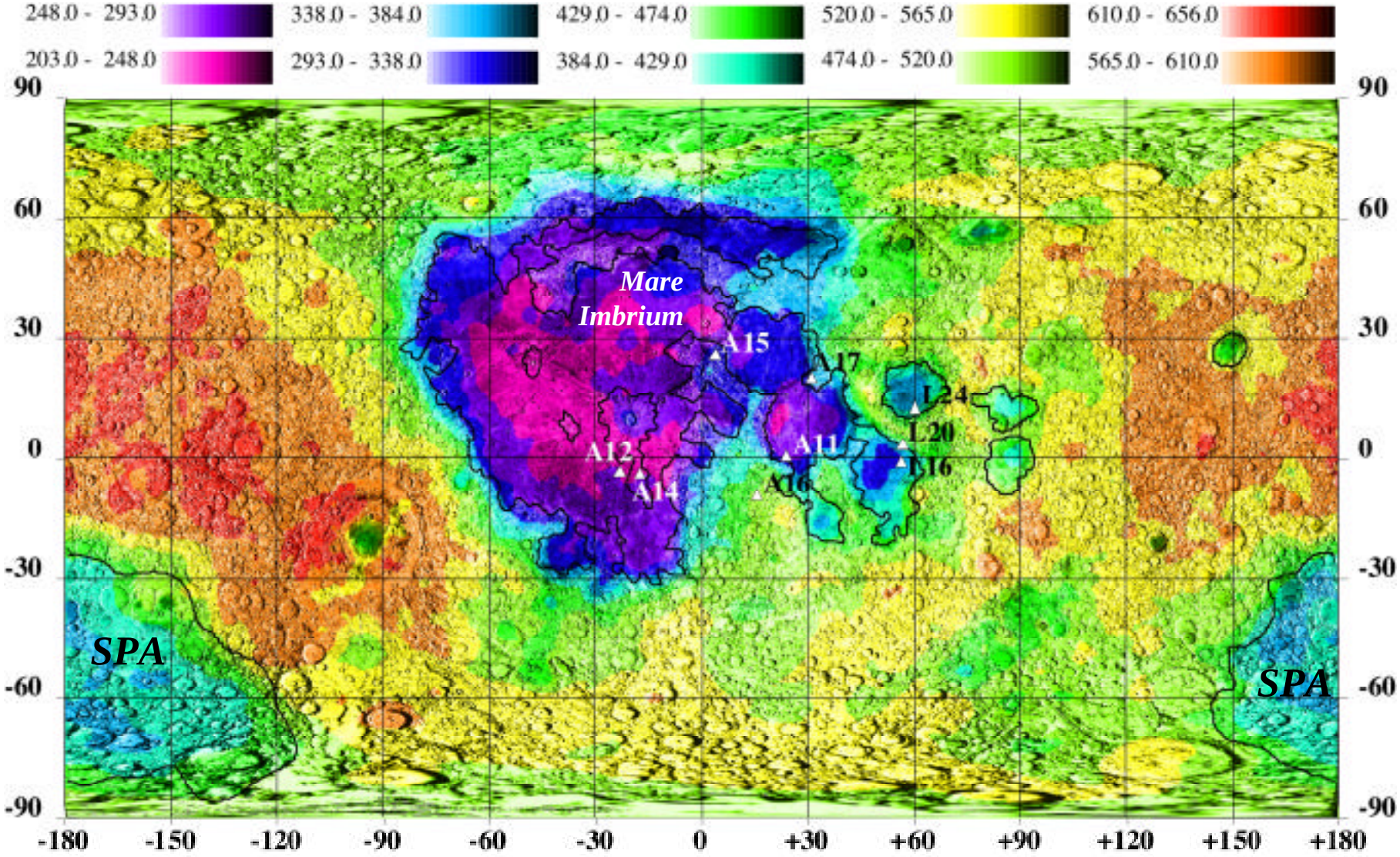

Figure 2a

Epithermal Neutron counts/32 sec

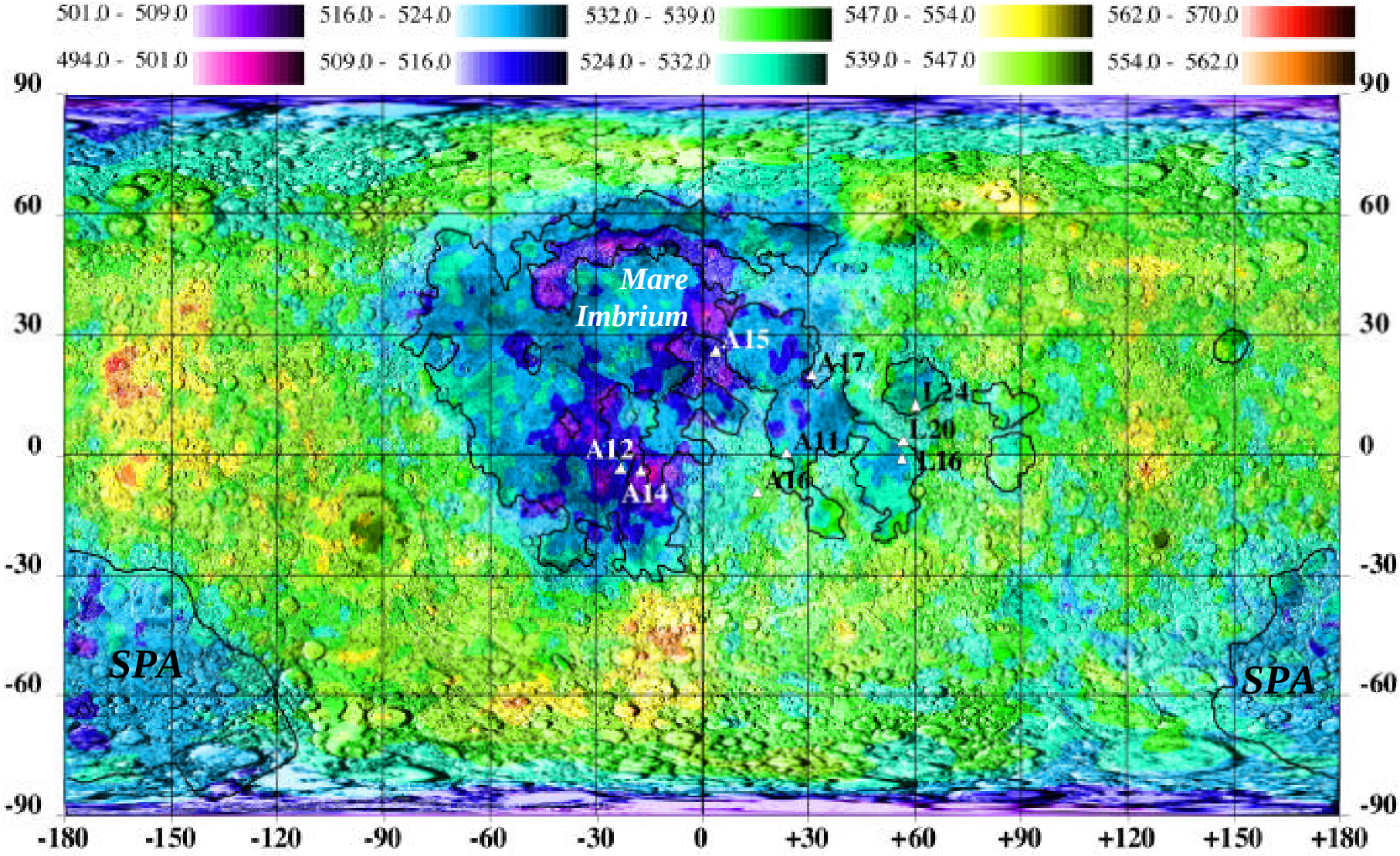

Figure 2b

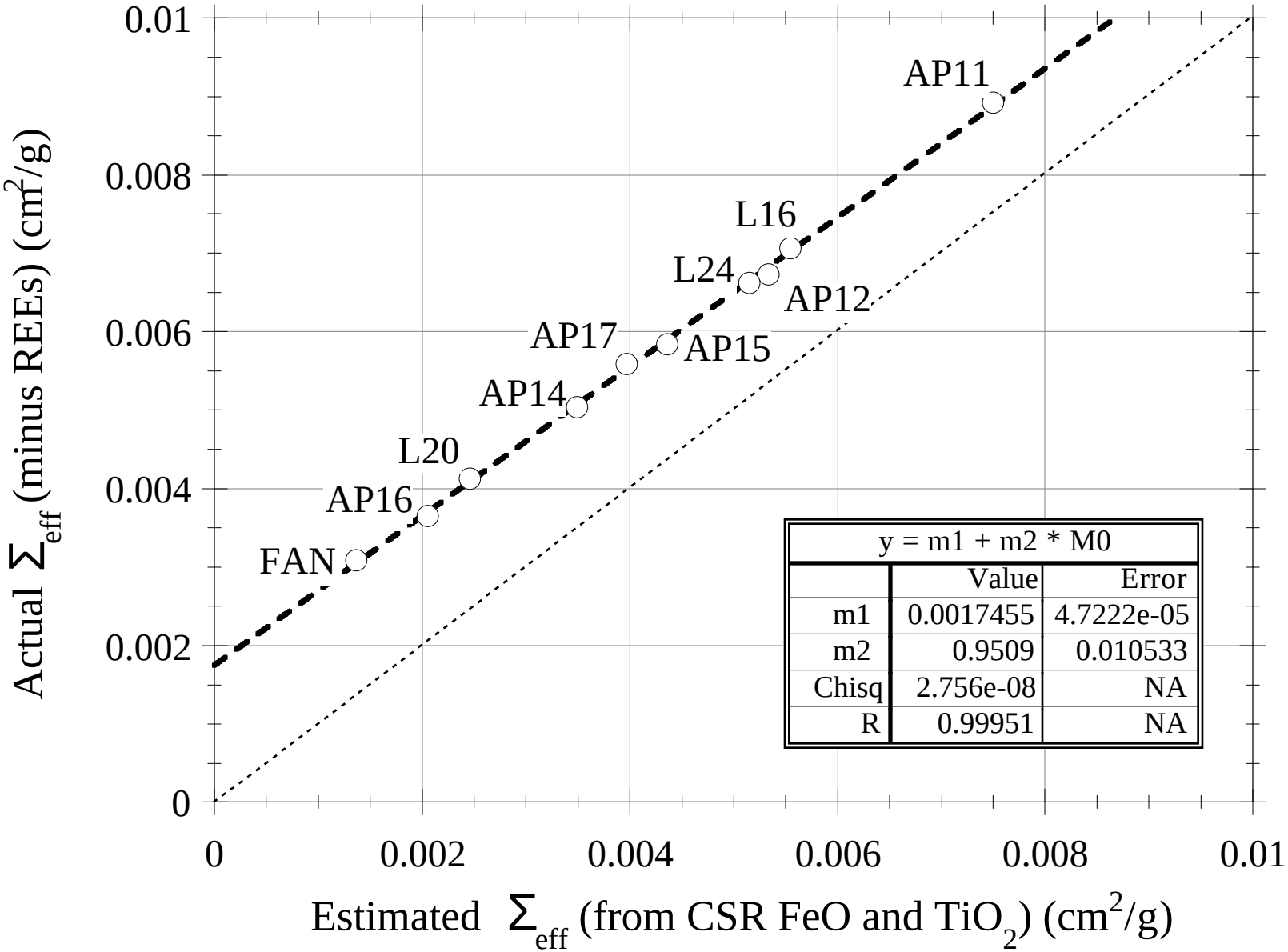
0.01
0.008
0.006
0.004
0.002
0
0
0.002
0.004
0.006
0.008
0.01
Actual Σ_{eff} (minus REEs) (cm^2/g)
Estimated Σ_{eff} (from CSR FeO and TiO_2) (cm^2/g)
AP11
L16
L24
AP12
AP17
AP15
AP14
L20
AP16
FAN
y = m1 + m2 * M0
Value
Error
m1
0.0017455
4.7222e-05
m2
0.9509
0.010533
Chisq
2.756e-08
NA
R
0.99951
NA

Fig. 3

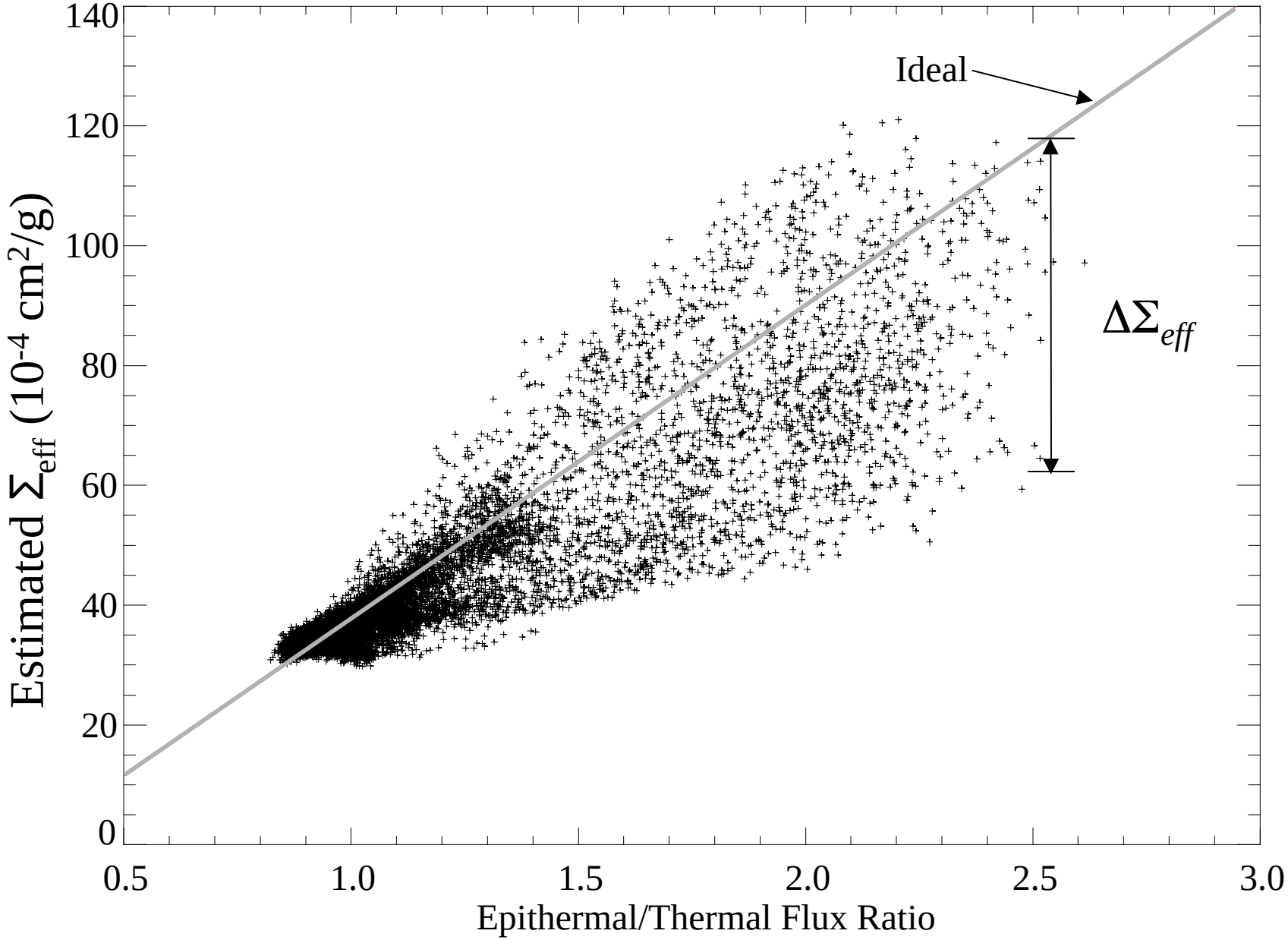
Ideal
$\Delta\Sigma_{eff}$
Estimated Σ_{eff} (10^{-4} cm^2/g)
Epithermal/Thermal Flux Ratio
0
20
40
60
80
100
120
140
0.5
1.0
1.5
2.0
2.5
3.0

Figure 4

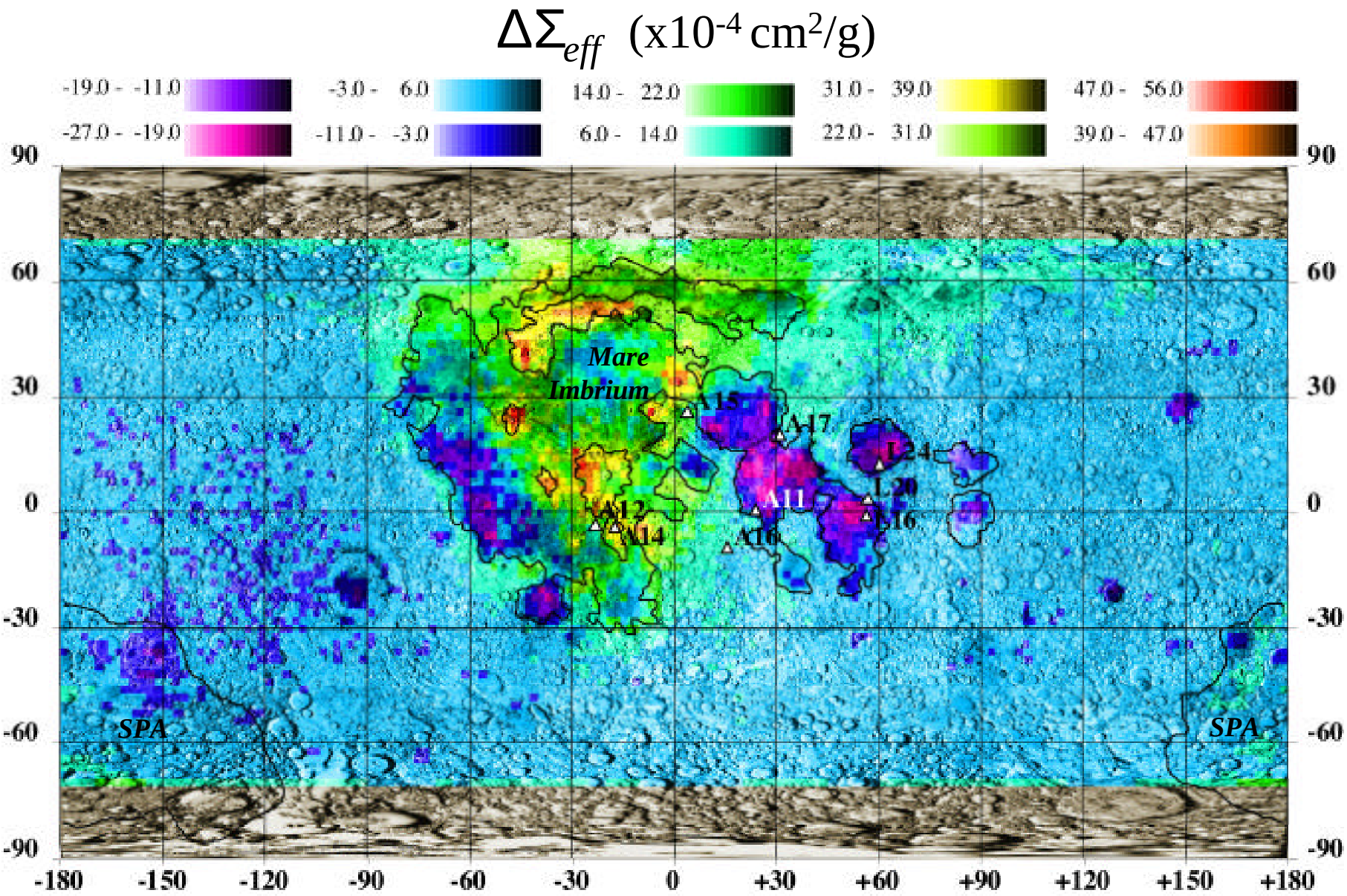
$\Delta\Sigma_{eff}$ (x10^{-4} cm^2/g)
-19.0 - -11.0
-27.0 - -19.0
-3.0 - 6.0
-11.0 - -3.0
14.0 - 22.0
6.0 - 14.0
31.0 - 39.0
22.0 - 31.0
47.0 - 56.0
39.0 - 47.0
Mare Imbrium
A15
A17
L24
L20
L16
A11
A16
A12
A14
SPA
SPA
90
60
30
0
-30
-60
-90
-180
-150
-120
-90
-60
-30
0
+30
+60
+90
+120
+150
+180

Figure 5

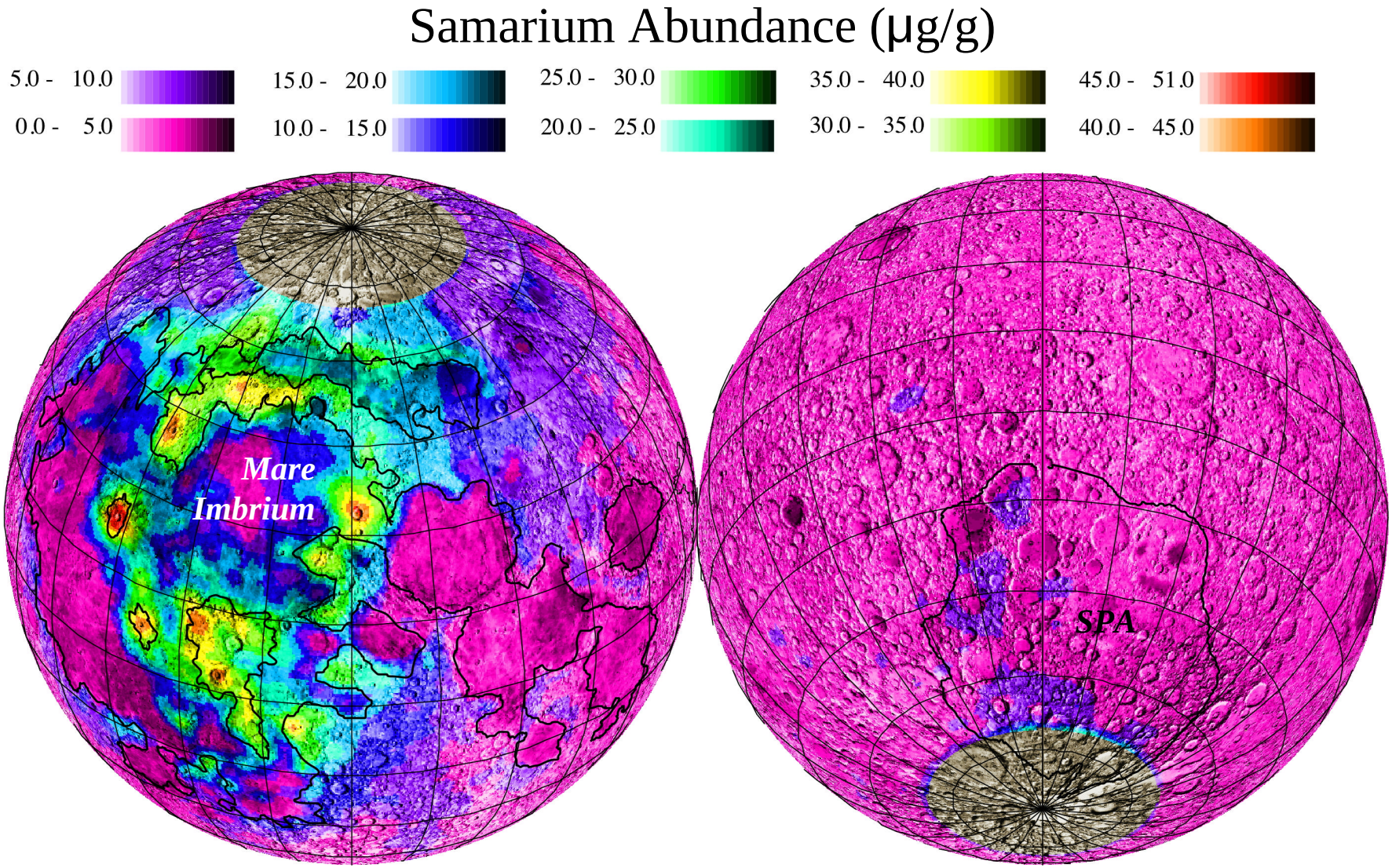
Samarium Abundance (µg/g)
5.0 - 10.0
0.0 - 5.0
15.0 - 20.0
10.0 - 15.0
25.0 - 30.0
20.0 - 25.0
35.0 - 40.0
30.0 - 35.0
45.0 - 51.0
40.0 - 45.0
Mare
Imbrium
SPA

Figure 6

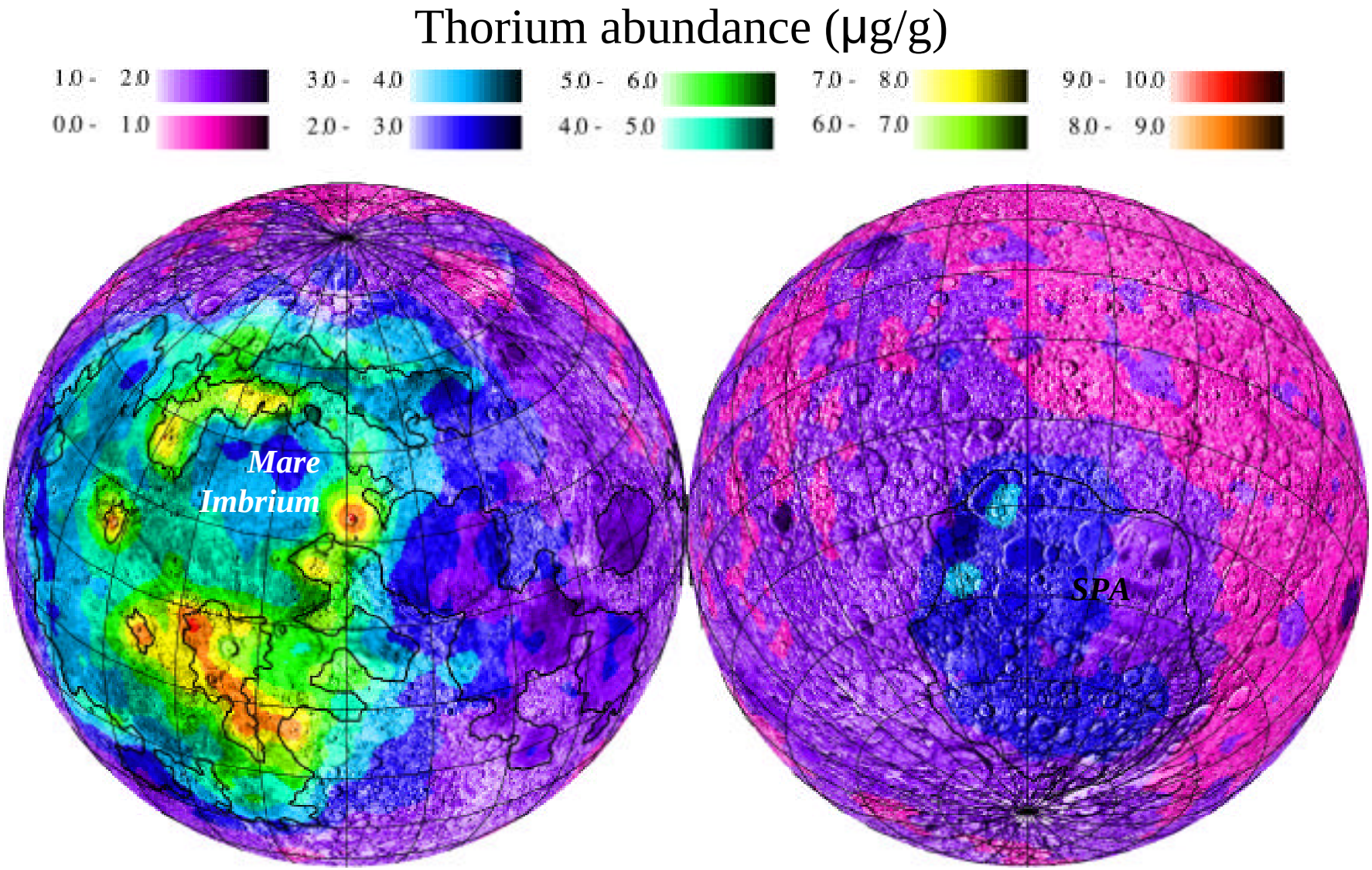
Thorium abundance (µg/g)
1.0 - 2.0
0.0 - 1.0
3.0 - 4.0
2.0 - 3.0
5.0 - 6.0
4.0 - 5.0
7.0 - 8.0
6.0 - 7.0
9.0 - 10.0
8.0 - 9.0
Mare Imbrium
SPA

Figure 7

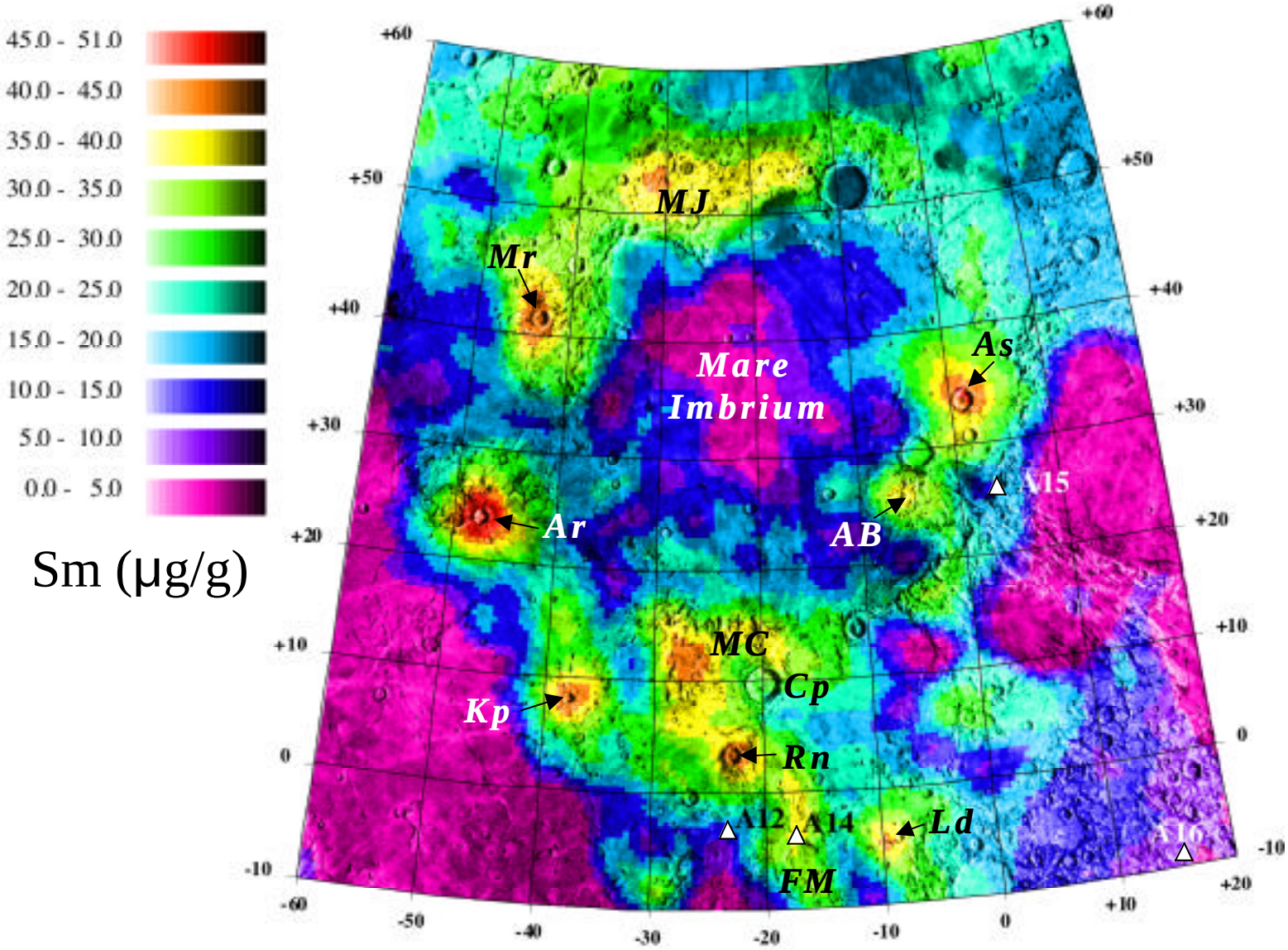
45.0 - 51.0
40.0 - 45.0
35.0 - 40.0
30.0 - 35.0
25.0 - 30.0
20.0 - 25.0
15.0 - 20.0
10.0 - 15.0
5.0 - 10.0
0.0 - 5.0
Sm (µg/g)
MJ
Mr
Mare Imbrium
As
A15
Ar
AB
MC
Cp
Kp
Rn
A12
A14
Ld
FM
A16
+60
+50
+40
+30
+20
+10
0
-10
-60
-50
-40
-30
-20
-10
0
+10
+20

Figure 8

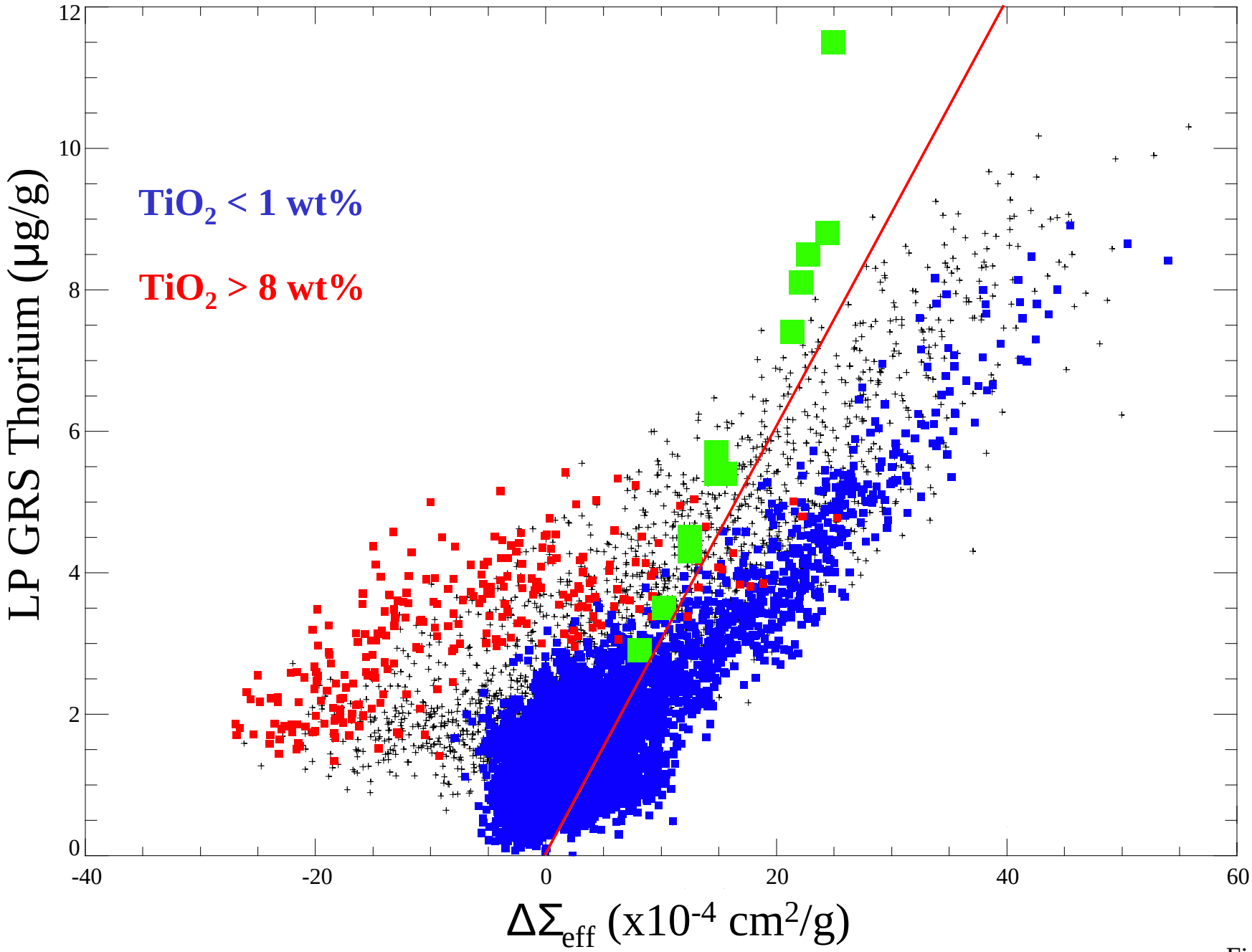
TiO2 < 1 wt%
TiO2 > 8 wt%
LP GRS Thorium (µg/g)
ΔΣeff (x10-4 cm2/g)
12
10
8
6
4
2
0
-40
-20
0
20
40
60

Figure 9

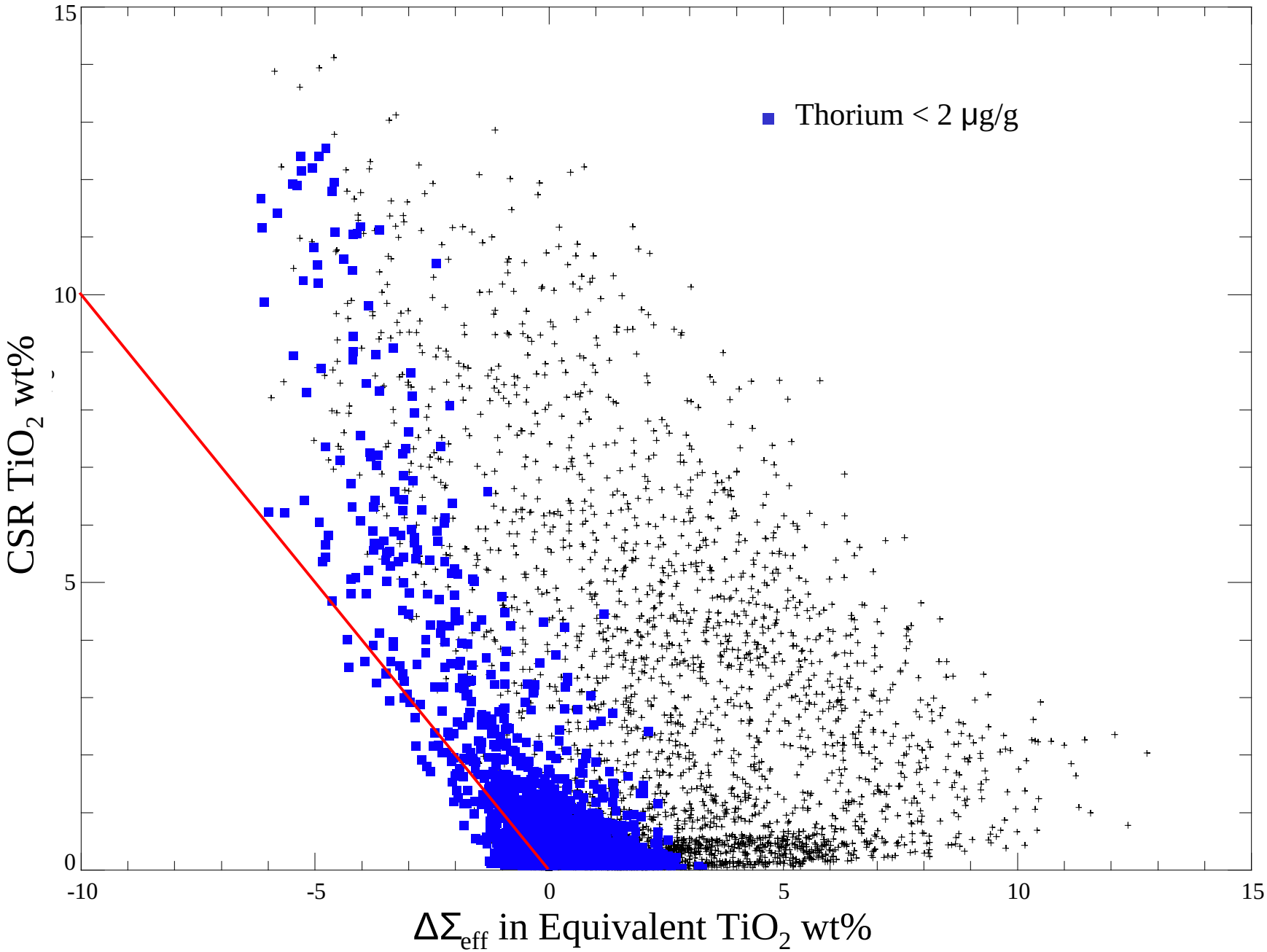
Thorium < 2 μg/g
CSR TiO_2 wt%
$\Delta\Sigma_{eff}$ in Equivalent TiO_2 wt%
15
10
5
0
-10
-5
0
5
10
15

Figure 10